# Deterministic bulk-boundary correspondences for skin and edge modes in a general two-band non-Hermitian system

Chong Hou,[1] Lingfang Li,[1] Shihua Chen,[1,2,*] Yi Liu,[3,4] Luqi Yuan,[5,†] Yiqi Zhang,[6,‡] and Zhenhua Ni[1,2,§]

[1]*School of Physics and Frontiers Science Center for Mobile Information Communication and Security, Southeast University, Nanjing 211189, China*

[2]*Purple Mountain Laboratories, Nanjing 211111, China*

[3]*Shanghai Key Lab of Modern Optical System, University of Shanghai for Science and Technology, Shanghai 200093, China*

[4]*CAS Center for Excellence in Ultra-Intense Laser Science, Shanghai 201800, China*

[5]*State Key Laboratory of Advanced Optical Communication Systems and Networks, School of Physics and Astronomy, Shanghai Jiao Tong University, Shanghai 200240, China*

[6]*Key Laboratory for Physical Electronics and Devices of the Ministry of Education & Shaanxi Key Lab of Information Photonic Technique, School of Electronic Science and Engineering, Faculty of Electronic and Information Engineering, Xi'an Jiaotong University, Xi'an 710049, China*

(Received 4 August 2022; revised 6 December 2022; accepted 13 December 2022; published 29 December 2022)

In isolated Hermitian systems, the bulk-boundary correspondence is generally thought of as a compelling principle guiding the occurrence of robust edge states through the topological invariants of the bulk. However, in open non-Hermitian systems that support non-Hermitian skin effects, the universality of the bulk-boundary correspondence has so far remained disputable in spite of being subjected to intensive studies. Here we provide analytical and numerical evidence of bulk-boundary correspondences for both skin and edge modes in 1D two-band non-Hermitian systems within the framework of a prototypical non-Hermitian Su-Schrieffer-Heeger model. Two different topological winding numbers, one on a Brillouin zone and the other on a generalized Brillouin zone, are defined to fully characterize the topological phases of matter and to understand such deterministic correspondences. In addition to the exact solutions for bulk states, we also obtain explicit solution forms for edge modes along with analytical conditions for their existence and localization, all exhibiting remarkable agreement with numerical results. Our results solve the elusive non-Hermitian topology and may facilitate experimental investigations of bulk-boundary correspondence in a wide range of non-Hermitian systems.

DOI: 10.1103/PhysRevResearch.4.043222

## I. INTRODUCTION

While Hermiticity enjoys a prominent status in quantum mechanics, non-Hermitian physics has attracted growing interest in both theoretical and experimental studies [1–8] intended for a wide range of classical [9–14] and quantum [15–19] systems. Particularly, when non-Hermiticity meets the concept of topology [20–28], there are emerging fruitful results such as non-Hermitian topological phases of matter [29–33], non-Hermitian topological insulators [34,35], non-Hermitian bulk-boundary correspondence (BBC) [36–40], and others [41–48]. Among them, the non-Hermitian skin effect [49–56] is an exotic phenomenon that has no Hermitian counterparts, where the eigenstates of the bulk could be mostly localized at boundaries under the open boundary condition (OBC) [57–59]. Obviously, because of this intrinsic skin effect, the observation of the edge states, which, as the name implies, host largely on the boundary as well [60–62], becomes extremely challenging from an experimental point of view [54,63].

When dealing with non-Hermitian topological phases, there is also a tough problem in that both the eigenvalues and eigenvectors can coalesce at an exceptional point (EP) (also known as branch-point singularity) [64,65]. As a result, the non-Hermitian Hamiltonian matrix becomes defective and nondiagonalizable at EPs [8], thus hindering the accurate numerical calculation of its eigenvalues and the corresponding eigenvectors near EPs, not to say of the precise identification of the bulk topological invariants [66–69]. In the vicinity of EPs, the non-Hermitian system behaves as if it loses its dimensionality [64] and thus brings about many nontrivial effects such as unidirectional lasing [70], enhanced sensing [71], formation of a bulk Fermi arc [13], and so on [7,11,27].

Considering these difficulties, the BBC, which has related robust edge states to bulk topological invariants with success in closed systems, is hard to verify for open non-Hermitian systems both in theory [72,73] and in experiments [37,38].

*cshua@seu.edu.cn
†yuanluqi@sjtu.edu.cn
‡zhangyiqi@xjtu.edu.cn
§zhni@seu.edu.cn

Up to now, it has still been debated whether the BBC works in non-Hermitian systems [42–44,74]. Nevertheless, to consummate the existing theory, there is research putting forward the concept of a generalized Brillouin zone (GBZ) on which a generalized or non-Bloch BBC is established for exploring edge states in non-Hermitian systems [49,68]. Recently, similar correspondence between the emergence of skin modes under OBC and the winding of the energy under periodic boundary condition (PBC) was proposed, revealing the topological origin of the non-Hermitian skin effect [52,58]. These investigations shed fresh light on identifying the non-Hermitian topological phases of matter, but how to precisely apply the related ideas to two-band non-Hermitian systems is still an open question worthy of further study.

In this paper, we consider a prototypical model for studying two-band non-Hermitian topological physics, namely, the one-dimensional (1D) non-Hermitian Su-Schrieffer-Heeger (SSH) model, which was widely used to mimic such systems as polyacetylene [75], photonic lattices [76,77], resonator arrays [78–80], electrical circuits [43,81,82], and nitrogen-vacancy centers in a diamond [83]. Within this SSH framework, we present the analytical and numerical evidence of deterministic BBCs for both skin and edge modes in 1D two-band non-Hermitian systems. Note here that we have generalized the terminology BBC to designate the *correspondence* between the states that host primarily on the *boundary* (say, edge modes or skin modes) and the topological invariants of the *bulk* that are obtained under the OBC or PBC. The BBCs will be referred to as being *deterministic* if the existence domain and localization for the edge or skin modes can be read from the topological invariants only. The subtlety of these two BBCs is that the topological winding number for skin modes is defined on the BZ, while the one for edge modes is defined on the GBZ, both of which have been improved distinctively as compared to previous studies [49,52,58,72]. In particular, to confirm the BBC that governs the nontrivial behaviors of edge states, we derive explicit edge-mode solutions and the conditions for their existence and localization, which agree well with the numerical results. It turns out that our analytical solutions could give one a clear picture of the non-Hermitian skin effect and topologically protected edge states. In this regard, the current paper helps probe deeply into the essence of the BBC and may solve once and for all the topology in two-band non-Hermitian systems.

## II. NON-HERMITIAN SSH MODEL AND ANALYTICAL SOLUTIONS

We start with considering the following Hamiltonian of the non-Hermitian SSH model under the OBC

$$\hat{H} = \sum_{n=1}^{N}(t_{1L}\hat{c}_{nA}^{\dagger}\hat{c}_{nB} + t_{1R}\hat{c}_{nB}^{\dagger}\hat{c}_{nA}) + \sum_{n=1}^{N-1}[t_{2L}\hat{c}_{nB}^{\dagger}\hat{c}_{(n+1)A} + t_{2R}\hat{c}_{(n+1)A}^{\dagger}\hat{c}_{nB} + t_{3L}\hat{c}_{nA}^{\dagger}\hat{c}_{(n+1)B} + t_{3R}\hat{c}_{(n+1)B}^{\dagger}\hat{c}_{nA}], \quad (1)$$

which describes an open tight-binding chain of $N$ cells involving asymmetric long-range hoppings [see Fig. 1(a)]. Here $\hat{c}_{nA(B)}$ is an annihilation operator of a particle on sublattice A (B) of the unit cell $n$, $t_{sL,R} \in \mathbb{R}$ are imbalanced hopping amplitudes in the same cell ($s = 1$) or between adjacent cells ($s = 2, 3$). For the sake of simplicity, we have ignored the non-Hermitian gain and loss on the A and B sublattice sites and let $t_{2L(R)}$, $t_{3L(R)} \geqslant 0$. Obviously, for these nonreciprocal hopping parameters $t_{sL,R}$, the real-space Hamiltonian Eq. (1) would exhibit non-Hermiticity, but respect a sublattice (or chiral) symmetry, namely, $\Gamma\hat{H}\Gamma^{-1} = -\hat{H}$, where $\Gamma = \bigoplus_n \sigma_{z,n}$ is the direct sum of $z$-component Pauli operator $\sigma_{z,n} = \mathrm{diag}(1, -1)$ [24,49,72]. Therefore, if $\hat{H}$ has an eigenvector $|\psi\rangle$ with eigenvalue $E$, then $\Gamma|\psi\rangle$ is also an eigenvector with eigenvalue $-E$.

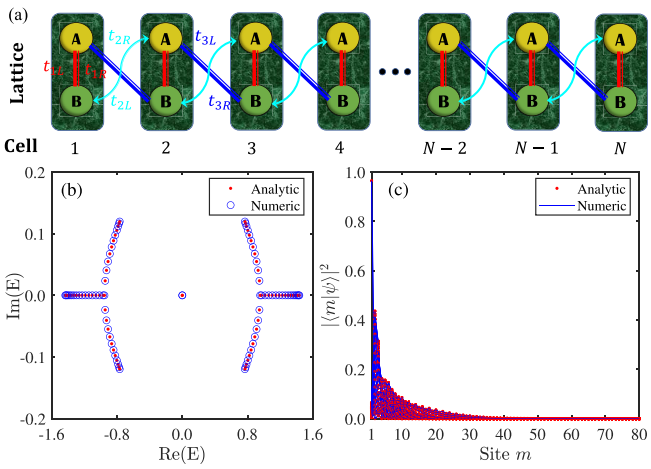


FIG. 1. (a) Geometry of a 1D non-Hermitian SSH model consisting of $N$ cells, with $t_{1L(R)}$ (red double line), $t_{2L(R)}$ (cyan line), and $t_{3L(R)}$ (blue double line) being nonreciprocal hopping parameters between sublattices A and B in the same cell or in adjacent cells. (b) and (c) show, respectively, the energy spectra and eigenfunctions of the Hamiltonian Eq. (1) with $N = 40$ for given parameters $t_{1L} = 3/8$, $t_{1R} = 1/8$, $t_{2L} = 10/9$, $t_{2R} = 8/9$, $t_{3L} = 2/9$, and $t_{3R} = 8/45$. Red dots: analytical solutions; blue circles or lines: numerical results.

Because of translation invariance of the bulk, the generalized Bloch Hamiltonian $\mathcal{H}(\beta)$ can be obtained as [84]

$$\mathcal{H}(\beta) = \begin{bmatrix} 0 & R_+(\beta) \\ R_-(\beta) & 0 \end{bmatrix}, \quad (2)$$

where $R_+(\beta) = t_{2R}/\beta + t_{1L} + t_{3L}\beta$ and $R_-(\beta) = t_{2L}\beta + t_{1R} + t_{3R}/\beta$. The eigenvalue equation reads

$$R_+(\beta)R_-(\beta) - E^2 = 0, \quad (3)$$

which is a quartic equation of the complex variable $\beta = e^{ik}$ with $k \in \mathbb{C}$. We should point out that when $k \in [0,\ 2\pi] \in \mathbb{R}$, Eq. (3) can give exactly the spectrum of Hamiltonian Eq. (1) under the PBC (see Appendix A). As will be shown later, this PBC spectrum would exhibit a topological property with respect to any base energy (excluding zero energy) on the OBC spectrum, which can be used to define the BBC for skin modes.

Basically, one can solve the real-space eigenvalue equation $\hat{H}|\psi\rangle = E|\psi\rangle$ exactly in the matrix form (see Appendix B). Here we employ the tensor product basis $|n, \alpha\rangle = |n\rangle_\alpha \otimes |\alpha\rangle \equiv |m\rangle$, where $|n\rangle_\alpha = \hat{c}_{n\alpha}^{\dagger}|0\rangle_\alpha$ stands for the excited state at the cell $n$, $\alpha \in \{A, B\}$, and $m = 1, 2, \cdots, 2N$ denotes the lattice site in the specified order $(1A, 1B, 2A, 2B, \cdots, NA, NB)$. In this basis, the

eigenvectors $|\psi\rangle$ can be defined by $|\psi\rangle = \sum_{m=1}^{2N} \psi_m |m\rangle = (\psi_{1A}, \psi_{1B}, \cdots, \psi_{NA}, \psi_{NB})^{\mathrm{T}}$ (T means transpose), where

$$\psi_{nA} = \frac{1}{E}\sum_{j=1}^{4} c_j R_+(\beta_j)\beta_j^n, \quad \psi_{nB} = \sum_{j=1}^{4} c_j \beta_j^n, \tag{4}$$

with $\beta_j$ ($j = 1, \cdots, 4$) being four roots of the quartic Eq. (3) for specified energy $E$ and $c_j$ four complex size-dependent coefficients. Obviously, for $c_j$ to be nontrivial, $\beta_j$ must obey the following boundary condition:

$$\begin{aligned}&\beta_{12}\beta_{34}[(\beta_1\beta_2)^{N+1} + (\beta_3\beta_4)^{N+1}] - \beta_{13}\beta_{24}[(\beta_1\beta_3)^{N+1} \\ &+ (\beta_2\beta_4)^{N+1}] + \beta_{14}\beta_{23}[(\beta_1\beta_4)^{N+1} + (\beta_2\beta_3)^{N+1}] = 0,\end{aligned} \tag{5}$$

where $\beta_{ij} = (\beta_i - \beta_j)(\beta_i\beta_j - t_{2R}/t_{3L})$. Hence, the coefficients $c_j$ in Eqs. (4) need to take

$$c_1 = \frac{\beta_1\left(\beta_{34}\beta_2^{N+2} + \beta_{23}\beta_4^{N+2} - \beta_{24}\beta_3^{N+2}\right)c_3}{\beta_3\left(\beta_{24}\beta_1^{N+2} - \beta_{14}\beta_2^{N+2} + \beta_{12}\beta_4^{N+2}\right)}, \tag{6}$$

$$c_2 = -\frac{\beta_2\left(\beta_{34}\beta_1^{N+2} + \beta_{13}\beta_4^{N+2} - \beta_{14}\beta_3^{N+2}\right)c_3}{\beta_3\left(\beta_{24}\beta_1^{N+2} - \beta_{14}\beta_2^{N+2} + \beta_{12}\beta_4^{N+2}\right)}, \tag{7}$$

$$c_4 = -\frac{\beta_4\left(\beta_{23}\beta_1^{N+2} + \beta_{12}\beta_3^{N+2} - \beta_{13}\beta_2^{N+2}\right)c_3}{\beta_3\left(\beta_{24}\beta_1^{N+2} - \beta_{14}\beta_2^{N+2} + \beta_{12}\beta_4^{N+2}\right)}, \tag{8}$$

with $c_3$ being a free constant used to normalize the eigenvector $|\psi\rangle$ such that $\langle\psi|\psi\rangle = 1$.

No doubt, Eq. (3) is a solvable quartic equation of $\beta$ for given energy $E$, and hence its four roots $\beta_j$ can be given by radicals, each depending on $E$. Insertion of these four roots into the boundary condition Eq. (5) could yield the allowed value of $E$, for given set of system parameters and the lattice size $N$. Once an energy value $E$ is known, all four $\beta_j$ are uniquely determined and, as a result, the corresponding eigenstate of the Hamiltonian Eq. (1) is uniquely obtained, by means of Eqs. (4), (6)–(8). As the energy $E$ allowed by Eq. (5) has $2N$ values, the number of the eigenstate $|\psi\rangle$ will also be $2N$, consistent with the dimensionality of Hamiltonian Eq. (1).

However, the above way for solving Eqs. (3) and (5) is only possible numerically, particularly for a large lattice size $N$. Below, we offer an analytical approach to solving this problem. For this end, one needs first to set

$$\beta_1 = re^{\frac{i}{2}(\Theta+\Phi-\Psi)}, \quad \beta_2 = re^{\frac{i}{2}(\Theta-\Phi+\Psi)}, \tag{9}$$

$$\beta_3 = re^{\frac{i}{2}(-\Theta+\Phi+\Psi)}, \quad \beta_4 = re^{-\frac{i}{2}(\Theta+\Phi+\Psi)}, \tag{10}$$

where $r$ is the real amplitude and $\Theta$, $\Phi$, and $\Psi$ are phase angles that can be complex. Substitution of Eqs. (9) and (10) into Eq. (3) yields, with the help of Vieta's theorem,

$$E^{\pm} = \pm\sqrt{\sum_{j=1}^{3} t_{jL}t_{jR} - 2r^2 t_{2L}t_{3L}(X + Y + Z)}, \tag{11}$$

$$\cos\left(\frac{\Theta}{2}\right)\cos\left(\frac{\Phi}{2}\right)\cos\left(\frac{\Psi}{2}\right) = -\frac{1}{8}\left(\frac{\mu}{r} + \nu r\right), \tag{12}$$

$$\sin\left(\frac{\Theta}{2}\right)\sin\left(\frac{\Phi}{2}\right)\sin\left(\frac{\Psi}{2}\right) = \frac{i}{8}\left(\frac{\mu}{r} - \nu r\right), \tag{13}$$

where $X = \cos\Theta$, $Y = \cos\Phi$, $Z = \cos\Psi$, $\mu = t_{1R}/t_{2L} + t_{1L}/t_{3L}$, $\nu = t_{1L}/t_{2R} + t_{1R}/t_{3R}$, and $r = [t_{2R}t_{3R}/(t_{2L}t_{3L})]^{1/4}$.

Substituting Eqs. (9) and (10) again into Eq. (5), we have a more explicit form for the boundary condition

$$\begin{aligned}&f(X)\cos[(N+1)\Theta](Y - Z) + f(Y)\cos[(N+1)\Phi] \\ &\times (Z - X) + f(Z)\cos[(N+1)\Psi](X - Y) = 0,\end{aligned} \tag{14}$$

where $f(x) = t_{3R}/t_{2L} + t_{2R}/t_{3L} - 2r^2x$. It is now obvious that by using the change of variables, the original Eqs. (3) and (5), which involve five variables $E$ and $\beta_j$, are simplified to Eqs. (12)–(14), which involve only three complex variables $\Theta$, $\Psi$, and $\Phi$. Once $\Theta$, $\Psi$, and $\Phi$ are worked out, the energy spectrum $E = (E^-, E^+)$ can be solely determined from Eq. (11).

Now, expressing $Y$ and $Z$ in terms of $X$ by use of Eqs. (12) and (13), and recalling that $\cos[(N+1)\Theta] = T_{N+1}(X)$, where $T_{N+1}(X)$ is a Chebyshev polynomial of the first kind [85], one can simplify Eq. (14) to a real-coefficient polynomial of $3N$ order about $X$, of course dropping the insignificant factors. Then, the $3N$ complex roots of this polynomial equation can be quickly located by computer routines, e.g., the command *root* in MATLAB software. Thanks to the symmetry hidden in Eq. (14), these $3N$ roots can be classified into $N$ groups, and each group has three members that take the same value of

$$X + \frac{(\mu/r + \nu r)^2}{16(X+1)} - \frac{(\mu/r - \nu r)^2}{16(X-1)}.$$

One can then choose one member as $X$, while let the other two be $Y$ and $Z$, respectively. As can be verified, all these $N$ solutions $(X, Y, Z)$ thus obtained would satisfy Eqs. (12)–(14).

Lastly, taking the inverse cosine of $(X, Y, Z)$, we get a set of complex angles $(\Theta, \Phi, \Psi)$, and hence a set of $\beta_j$ from Eqs. (9) and (10). At this step, one can reorder $\beta_{1,2,3,4}$ to fulfill $|\beta_1| \leqslant |\beta_2| \leqslant |\beta_3| \leqslant |\beta_4|$. Naturally, a substitution of $\beta_j$ together with the values of $c_j$ into Eqs. (4) could yield $N$ eigenvectors $|\psi\rangle$ of the Hamiltonian Eq. (1) that are associated to $E^+$ in Eq. (11) and $N$ eigenvectors $\Gamma|\psi\rangle$ that are associated to $E^-$. To facilitate discussion, we also sort the energy $E$ according to the rules as follows. We first divide the energy spectrum into real part $E_{\mathrm{re}}$ and complex part $E_{\mathrm{co}}$. Then, the real energy is sorted in ascending order according to its magnitude, while the complex energy is sorted according to its absolute value. The resultant energy spectrum is arranged, from left to right, as $(E_{\mathrm{re}}^-, E_{\mathrm{co}}^-, 0$ if exists, $E_{\mathrm{co}}^+, E_{\mathrm{re}}^+)$ in the complex energy plane. Of course, during this sortation operation, the eigenvector associated to $E$ needs also be sorted one by one.

The above procedures can solve Eqs. (3) and (5) elegantly for the sorted energy $E$, the sorted four roots $\beta_j$, and consequently the sorted eigenvectors by virtue of Eqs. (4), (6)–(8), for given hopping parameters $t_{sL(R)}$ and arbitrary lattice size $N \geqslant 2$. As an example, we present in Figs. 1(b) and 1(c) the analytical and numerical solutions for both the energy spectra and eigenfunctions of the Hamiltonian Eq. (1) with a lattice size $N = 40$, whose hopping parameters are specified in the caption. It is seen that our analytical solutions, indicated by red dots, agree well with the numerical ones, where blue circle stands for energy and blue lines for eigenvectors.

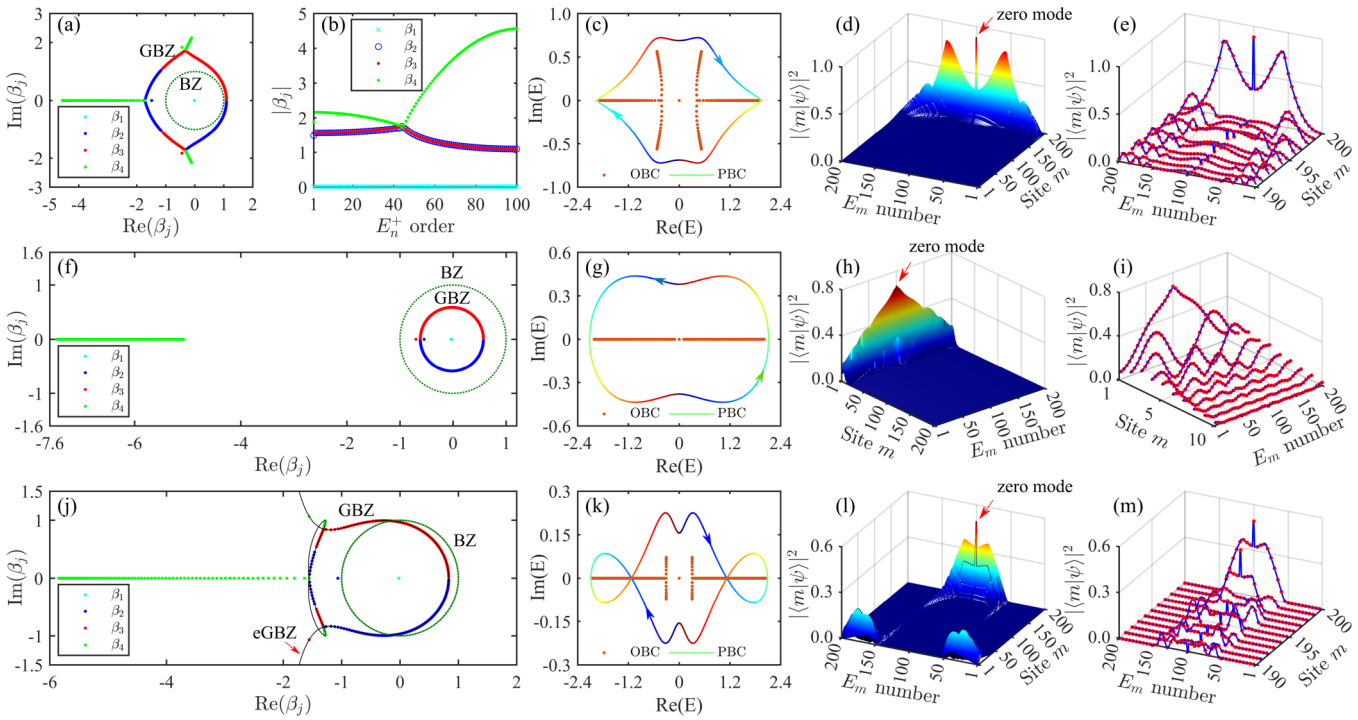


FIG. 2. The GBZ, energy spectra, and skin modes of the bulk obtained analytically under the OBC with $N = 100$, for (a)–(e): $t_{1L} = 1/5$, $t_{1R} = 9/5$; (f)–(i): $t_{1L} = 13/10$, $t_{1R} = 7/10$; and (j)–(m): $t_{1L} = 7/10$, $t_{1R} = 13/10$, while keeping the other hopping parameters the same, i.e., $t_{2L} = 6/5$, $t_{2R} = 4/5$, $t_{3L} = 9/40$, and $t_{3R} = 1/40$. The rightmost column demonstrates the comparison of our analytical solutions for the skin modes (blue curves) with the numerical solutions (red dots), zoomed within ten lattice sizes. Panel (b) gives the evolution of four $\beta_j$ with the energy ordinal number where $|\beta_2| = |\beta_3|$ occurs. The highest peaks in the 3D surface plots (d), (h), and (l) are identified as zero modes, which correspond to a zero energy located at origin in panels (c), (g), and (k). For comparison, we also present the auxiliary line of eGBZ in panel (j) and the energy spectra obtained under the PBC (colored solid lines) in (c), (g), and (k)

## III. NON-HERMITIAN SKIN EFFECT AND BBC FOR SKIN MODES

In Fig. 1(c), one also observes a typical non-Hermitian skin effect, which refers to the localization of bulk states on the boundary of an open chain. This phenomenon is counterintuitive from the conventional view of Bloch's theorem, which states that the bulk eigenstates are modulated plane waves [84] (see also Appendix A, where we present the exact bulk-mode solutions for the same Hamiltonian with PBC). Our analytical solutions Eqs. (4) clearly reveal that the emergence of such skin effect is attributed to the non-Hermiticity of Hamiltonian imposed by the OBC, and can be uniquely determined by the size and position of GBZ relative to the BZ (unit circle) of PBC in the complex plane. Generally, when Eq. (3) has four roots $\beta_i$ satisfying $|\beta_i| \leqslant |\beta_j|$ for $i < j$, the GBZ is constituted by the trajectories of $\beta_2$ and $\beta_3$ in the thermodynamic limit (i.e., $N \to \infty$), where $|\beta_2| = |\beta_3|$ holds [72]. Usually, one can calculate GBZ using a finite $N$ and basically, the larger the lattice size, the closer this GBZ gets to the exact GBZ (eGBZ), the latter of which can be expressed by elementary functions (see Appendix C). We find that for large enough $N$, the bulk modes will only be determined by $\beta_2$ and $\beta_3$ on the GBZ, as the contributions from both $\beta_1$ and $\beta_4$ become vanishingly small. Hence, the bulk modes will localize on the right end (right skin effect) if the GBZ embraces the BZ circle, but tend to localize on the left end (left skin effect) if the GBZ is inside the BZ circle. However, when the GBZ intersects the BZ circle, there will be more localizations of bulk modes on both ends (double skin effect). Figure 2 shows the analytical solutions demonstrating the right skin effect (see the top row), the left skin effect (see the middle row), and the double skin effect (see the bottom row), which correspond to a GBZ outside, inside, and intersecting the BZ circle, respectively, obtained with $N = 100$ and different sets of hopping parameters. For comparison, the numerical solutions for these bulk modes (red dots) are also provided on the rightmost column, which show a striking agreement with our analytical solutions (here we have enlarged the pictures within ten lattice sizes).

As a matter of fact, there is a topological origin responsible for these different kinds of non-Hermitian skin effects [52,58]. It depends strongly on the evolution of the energy spectrum obtained under PBC as the momentum traverses the BZ. For this reason, we also plot the PBC spectra (colored solid lines) in Figs. 2(c), 2(g), and 2(k) for the same hopping parameters, as the Bloch momentum $k$ runs from 0 to $2\pi$. It is seen that each PBC spectrum always traces a loop surrounding the OBC spectrum (red dots), with a direction depending on the choice of system parameters. This suggests a $\mathbb{Z}$ topological winding number intended for the skin mode of order $m$, defined by

$$w_m = \oint_{\mathrm{BZ}} \frac{dk}{2\pi i} \partial_k [\ln \det(\mathcal{H}(k) - E_m)], \tag{15}$$

where $\mathcal{H}(k)$ is given by Eq. (2) with $k \in [0,\ 2\pi]$, and $E_m \neq 0$ is the energy of the $m$th-order skin mode obtained with the

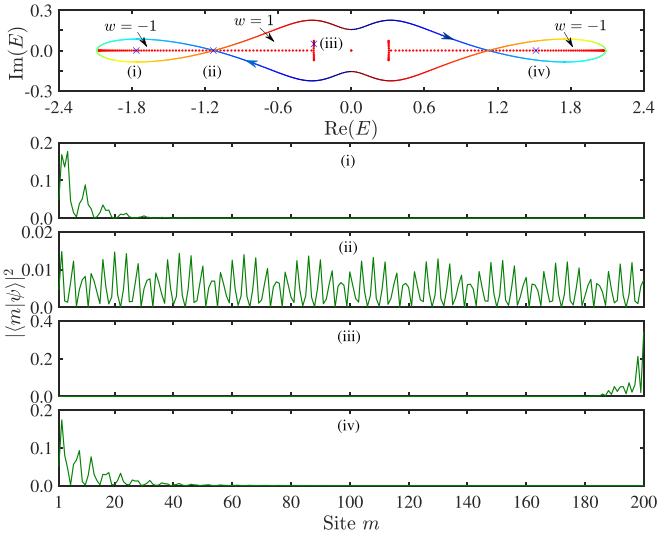


FIG. 3. BBC for skin modes concerning the third GBZ case of Fig. 2. Top panel: OBC (red dots) and PBC (colored solid line) energy spectra in the complex plane. (i)–(iv) Profiles of bulk states for the four base energy points (blue crosses) selected in the top panel.

OBC. Note that this definition outperforms those presented in Refs. [23,52,58], where the base energy $E_m$ is not forced on the OBC spectrum and hence the skin mode to be studied is not specified. We can now relate this winding number $w_m$ to the emergence of skin modes and hence term it *BBC for skin modes*. Specifically, when $w_m$ is a positive (negative) integer, which means that the PBC spectrum surrounds the base energy $E_m$ in a clockwise (counterclockwise) way, the skin mode associated to the energy $E_m$ will localize on the right (left) boundary of the chain. Of course, if $w_m = 0$, no skin mode will take place. To illustrate this, we take the third case in Fig. 2 as an example, which shows a slightly complicated PBC spectral structure. The winding number $w_m$ for any of the regions encompassed by the directed PBC spectrum curve can be easily calculated from Eq. (15), and has been indicated in the top panel of Fig. 3. Typically, four base energy points (blue crosses) are chosen from the OBC spectrum, which take the winding numbers (i) $w = -1$, (ii) $w = 0$, (iii) $w = 1$, and (iv) $w = -1$, respectively. The corresponding states are then plotted in panels (i)–(iv), which display left localization for $w = -1$, zero localization for $w = 0$, and right localization for $w = 1$, thereby justifying the BBC for skin modes. It is also suggested that in open non-Hermitian systems, not all bulk states are necessarily considered as skin modes; for instance, the bulk state that has an energy meeting the PBC spectrum will occupy extensively in the whole chain and is therefore not a genuine skin mode, as seen in panel (ii).

In addition to those shown in Fig. 2, our analytical solutions can also reveal other possibilities for GBZ and skin modes. Figure 4 shows an interesting case that was seldom seen before, namely, a case where the GBZ can intersect the BZ at six points [see Fig. 4(a)]. In this case, the bulk modes can exhibit a similar double skin effect as the energy varies,

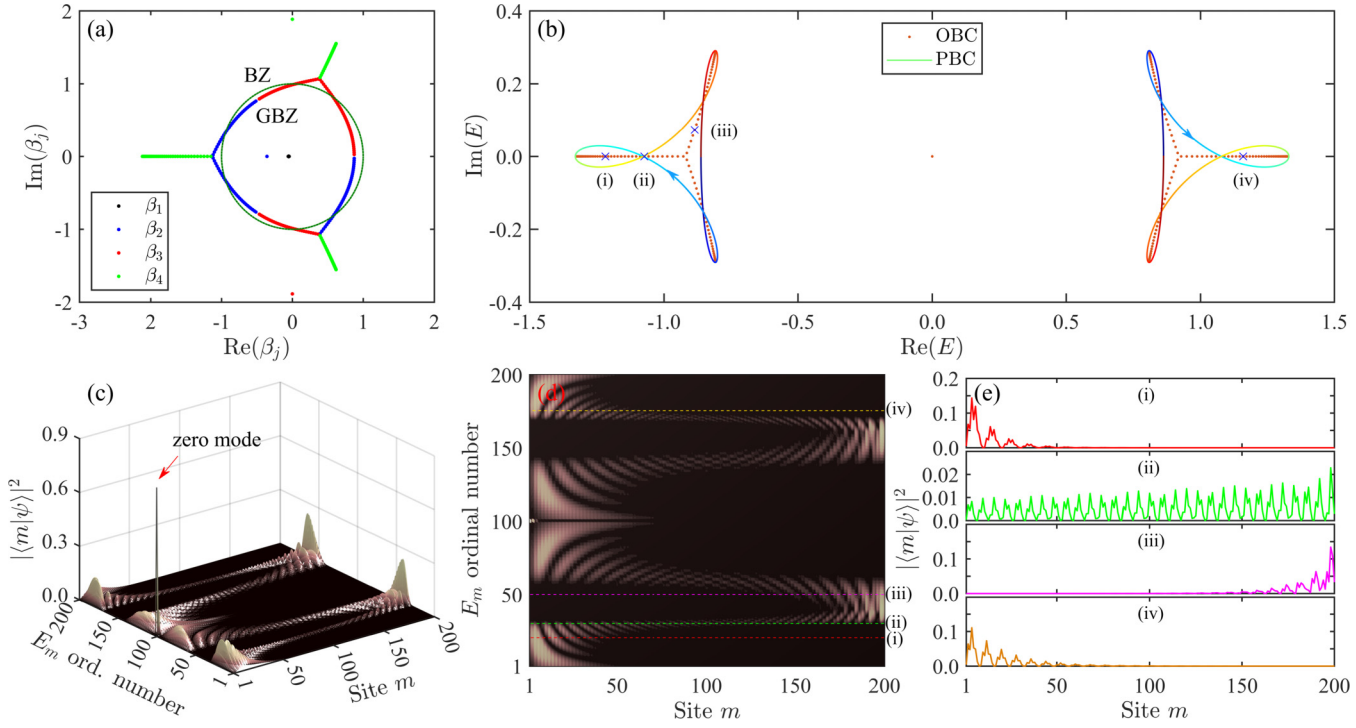


FIG. 4. Double skin effect of the bulk modes when the GBZ intersects the BZ circle at six points, occurring for $t_{1L} = 0$, $t_{1R} = 1/2$, $t_{2L} = 6/5$, $t_{2R} = 4/5$, $t_{3L} = 9/40$, and $t_{3R} = 1/40$. (a) GBZ, (b) OBC (red dots) and PBC (colored solid lines) energy spectra in the complex plane, (c) 3D surface plot of the modes, (d) the corresponding contour plot of the modes, and (e) the profiles of bulk modes for the four typical energy points (blue crosses) selected in (b). The red arrow in (c) indicates the zero (or edge) mode which is associated to the degenerate zero energy points in (b). The red, green, purple, and yellow dashed lines in (d) mark the bulk states of four selected energy points in (b).

but there are four localizations on the left end and two localizations on the right end, as seen in Figs. 4(c) and 4(d). More interestingly, it is exhibited that the PBC spectrum consists of two parts, each segmenting the OBC spectrum into four regions, but with the isolated zero energy point excluded [see Fig. 4(b)]. According to the heading direction of the PBC energy curve, one can easily obtain the winding number $w_m$ for any bulk mode within these regions. For example, for the four typical energy points (blue crosses) denoted by (i), (ii), (iii), and (iv) in Fig. 4(b), the winding number is equal to $w = -1$, 0, 1, and $-1$, respectively. Correspondingly, the bulk states at these energy points exhibit left, zero, right, and left localizations, as seen in Fig. 4(e). Once again, the results obtained are consistent with the BBC for skin modes established above.

## IV. EDGE STATES AND THE RELATED BBC

In Figs. 2(d), 2(h), 2(l), and 4(c), we have indicated the highest peaks by zero modes (see arrows therein), which have a degenerate zero energy in the complex energy plane. These zero modes tend to localize on the boundary, whether the systems are Hermitian or not, and thus are often termed edge modes. Although skin modes can also localize on the boundary, such edge modes intended for the two-band non-Hermitian systems are different from the former in that (1) the edge modes are nontrivial behaviors occurring at EPs and always possess a degenerate zero energy that is not allowed by the former and (2) the edge modes respect another BBC whose topological invariant is not defined by Eq. (15) but by [23,24]

$$W = \oint_{\mathrm{GBZ}} \frac{dk}{4\pi i} \mathrm{tr}(\mathcal{S}\mathcal{H}^{-1}\frac{d\mathcal{H}}{dk}), \tag{16}$$

where $\mathcal{H}(k)$ is still given by Eq. (2) but with $k = -i\ln\beta \in \mathbb{C}$, $\mathcal{S}$ is a unitary operator responsible for the sublattice (or chiral) symmetry, and tr denotes the trace of the matrix. As seen, this winding number can not be derived from Eq. (15) by taking $E_m = 0$. We should emphasize that the calculation of Eq. (16) is performed on the GBZ rather than on the BZ, as the latter would result in a fractional winding number implying the breakdown of BBC [24,42].

In the following, we show that, in the majority of parameter situations, the edge modes will primarily host on either boundary of the open chain and thus the topological invariant Eq. (16) can be improved by presuming $\mathcal{S} = \pm\sigma_z$, from which the localization hallmark of edge states can be accurately predicted, as occurred in one-band non-Hermitian systems (see, e.g., Fig. 2 in Ref. [23]). This formalism enables us to define a deterministic BBC for edge states—by *deterministic* we mean that the edge state localized on the left (right) boundary corresponds to the negative (positive) topological invariant, while the absence of edge state corresponds to zero one (i.e., $W = 0$).

To confirm the BBC for edge states on an analytical level, we need to find the explicit approximate edge-mode solutions, along with their existence and localization conditions. This process is not so trivial as what we did for the bulk-mode solutions, as edge modes are wave states occurring at the EPs where the vector space is severely skewed [64]. This is also seen from Eqs. (4), where the solutions would become indefinite as $E \to 0$. In fact, when $E = 0$, Eq. (3) has four roots $\beta'_{1,2} = (-t_{1R} \pm \sqrt{t_{1R}^2 - 4t_{2L}t_{3R}})/(2t_{2L})$, and $\beta'_{3,4} = (-t_{1L} \pm \sqrt{t_{1L}^2 - 4t_{2R}t_{3L}})/(2t_{3L})$. One can sort these roots according to their moduli and rename them from least to greatest by $\beta_1^e$, $\beta_2^e$, $\beta_3^e$, and $\beta_4^e$. We find that when $|\beta_2^e\beta_3^e| < 1$, the edge modes will localize on the left end, and are given by

$$\psi_{nA}^{\mathrm{ed}} = \beta_{23}^e(\beta_1^e)^{n+1}R_+(\beta_1^e) - \beta_{13}^e(\beta_2^e)^{n+1}R_+(\beta_2^e), \quad \psi_{nB}^{\mathrm{ed}} = 0 \tag{17}$$

if $R_+(\beta_2^e) \neq 0$ or can be expressed by

$$\psi_{nA}^{\mathrm{ed}} = 0, \qquad \psi_{nB}^{\mathrm{ed}} = \beta_{23}^e(\beta_1^e)^{n+1} - \beta_{13}^e(\beta_2^e)^{n+1} \tag{18}$$

if $R_+(\beta_2^e) = 0$. Otherwise, for $|\beta_2^e\beta_3^e| > 1$, the edge modes tend to localize on the right boundary, with their solutions given by

$$\psi_{nA}^{\mathrm{ed}} = 0, \qquad \psi_{nB}^{\mathrm{ed}} = (\beta_3^e)^n - \left(\frac{\beta_3^e}{\beta_4^e}\right)^{N+1}(\beta_4^e)^n, \tag{19}$$

if $R_+(\beta_3^e) = 0$, or defined by

$$\psi_{nA}^{\mathrm{ed}} = (\beta_3^e)^n - \left(\frac{\beta_3^e}{\beta_4^e}\right)^{N+1}(\beta_4^e)^n, \qquad \psi_{nB}^{\mathrm{ed}} = 0, \tag{20}$$

if $R_+(\beta_3^e) \neq 0$. We should point out that for a special set of hopping parameters satisfying $|\beta_2^e\beta_3^e| = 1$, the zero modes would exhibit weak localization on both left and right boundaries, as compared to the skin modes of the bulk. The reason is that the GBZ will now be nearly tangent to the BZ circle, and thus the edge states formed would behave like the ones occurring in Hermitian systems whose wave functions may occupy both ends (see, e.g., Fig. 1.4 in Ref. [84]). In this paper, we shall not digress into this special situation but reserve it for detailed study in a subsequent work.

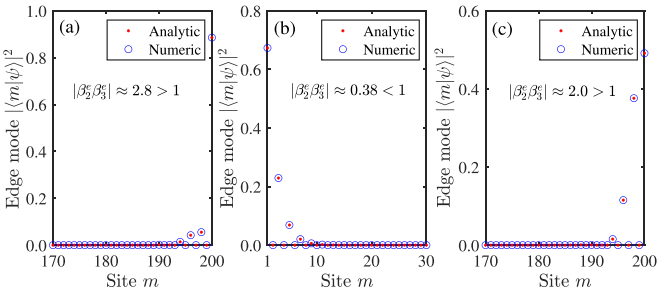


FIG. 5. Normalized edge states for the same three GBZ cases as in Fig. 2, with (a) GBZ outside BZ, (b) GBZ inside BZ, and (c) GBZ intersecting BZ. Red dots and blue circles denote the analytical and numerical solutions, respectively.

For illustration, we demonstrate in Fig. 5 the comparison of numerical edge modes of three GBZ cases in Fig. 2 with our analytical solutions Eqs. (17) and (19), all zoomed within 30 lattice sites. Remarkably, these analytical solutions as well as the analytical conditions for left or right localization can predict the edge modes precisely. We also confirm that the analytical solutions Eqs. (18) and (20) for other situations can coincide with numerical ones as well, provided that $|\beta_2^e\beta_3^e| \neq 1$ is met. It is clearly seen that these edge modes in the thermodynamic limit tend to host on either sublattice A or B,

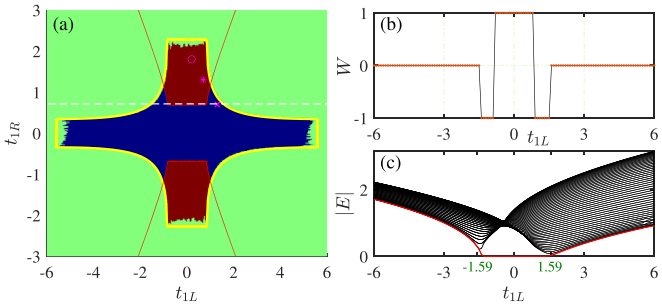


FIG. 6. (a) Map of winding number in the plane $(t_{1L}, t_{1R})$, where the red, blue, and green regions represent $W = 1, -1$, and 0, respectively, numerically obtained for $N = 50$ and $t_{2L} = 6/5$, $t_{2R} = 4/5$, $t_{3L} = 9/40, t_{3R} = 1/40$. The purple circle, cross, and asterisk indicate the three GBZ cases (from top to bottom) in Fig. 2, respectively. The yellow curves are specified by Eqs. (21) and (22), while the red curve is the demarcation line defined by $|\beta_2^e \beta_3^e| = 1$. (b) and (c) show the winding number $W$ and energy bands along the white dashed line in (a), where $t_{1R} = 7/10$.

not on both, in contrast to what happens in the open two-band Hermitian systems [84]. Only when $|\beta_2^e \beta_3^e| = 1$ is fulfilled would they host on both sublattice sites, but this case should be excluded from our theory established here, as stated above.

Concerning the domain that admits edge modes, one can resort to the BBC principle which relates edge states to the bulk winding number. Here we can find it analytically using the condition $|\beta_2^e| = |\beta_3^e|$, under which the edge modes begin to dissociate themselves from the bulk states [49]. The domain of edge modes can then be obtained as

$$t_{1R} = \pm \left[ \frac{t_{2L} t_{1L}}{t_{3L}} - \frac{2(t_{2L} t_{2R} - t_{3L} t_{3R})}{t_{1L} - \sqrt{t_{1L}^2 - 4 t_{2R} t_{3L}}} \right] \tag{21}$$

for $2\sqrt{t_{2R} t_{3L}} \leqslant t_{1L} \leqslant (t_{2L} t_{2R} + t_{3L} t_{3R})/\sqrt{t_{2L} t_{3R}}$, and

$$t_{1R} = \pm \left[ \frac{t_{2L} t_{1L}}{t_{3L}} - \frac{2(t_{2L} t_{2R} - t_{3L} t_{3R})}{t_{1L} + \sqrt{t_{1L}^2 - 4 t_{2R} t_{3L}}} \right] \tag{22}$$

for $-(t_{2L} t_{2R} + t_{3L} t_{3R})/\sqrt{t_{2L} t_{3R}} \leqslant t_{1L} \leqslant -2\sqrt{t_{2R} t_{3L}}$.

Figure 6(a) illustrates the phase diagram of winding number obtained numerically with $N = 50$, according to the winding number formalism Eq. (16). We have designated the left localization by $W = -1$ (blue region), the right localization by $W = 1$ (red region), and the zero localization by $W = 0$ (green region). The corresponding winding number $W$ and the energy bands along the white dashed line (i.e., $t_{1R} = 7/10$) have been displayed in Figs. 6(b) and 6(c). It is clearly seen that the regions of nonzero winding number are very consistent with the domain of edge modes defined by Eqs. (21) and (22) (see yellow curves), and the demarcation line between positive and negative winding numbers almost coincides with that defined by $|\beta_2^e \beta_3^e| = 1$ (see red curve). The only discrepancy lying in four ends of domain is caused by numerical errors of calculation of the winding number near EPs and a relatively small lattice size ($N = 50$) used. Such errors can be reduced significantly by increasing the decimal number of digits and the lattice size $N$ to a very high value, but of course at the cost of an enormous amount of computing time. The three GBZ cases shown in Fig. 2 are indicated by purple circle, cross, and asterisk, which all exhibit consistency with numerical results of the winding number. Therefore, the non-Bloch BBC for edge modes has been unequivocally confirmed. Moreover, our results suggest that when choosing $\mathcal{S} = \sigma_z$ for $|\beta_2^e \beta_3^e| > 1$ and $\mathcal{S} = -\sigma_z$ for $|\beta_2^e \beta_3^e| < 1$, the topological winding number defined by Eq. (16) can correctly predict both the existence and localization of edge modes in two-band non-Hermitian systems. The only exception is what takes plane on the demarcation line $|\beta_2^e \beta_3^e| = 1$ where only the existence domain of edge modes could be predicted by the winding number Eq. (16).

## V. CONCLUSION

We confirmed, on an analytical level, the BBC for skin modes and the BBC for edge modes in a 1D two-band non-Hermitian system within the framework of a universal non-Hermitian SSH model. There are several major conclusions to be drawn here. First, an analytical approach to solving such an intricate SSH model for energy spectra and eigenstates was put forward, which not only breaks through the limitations of those used in Refs. [49,72,73], but also offers a strong reference for solving other 1D one- or multiband non-Hermitian models, no matter how complicated the hopping parameters involved. In fact, the importance of such analytical studies can not be overemphasized, as they enable one to identify and understand the key factors that lead to the non-Hermitian skin effects, EPs, the formation of edge states, and even the BBC.

Second, we demonstrated unequivocally a deterministic BBC for either skin or edge modes, by introducing two distinct topological winding numbers that have been improved distinctively in contrast to those extensively used in previous studies [23,24,49,52,58,72]. Any indiscriminate use of the above two topological invariants could result in a failure of BBC in non-Hermitian systems.

Last but not least, we provided the explicit analytical solutions for the edge modes, as well as the analytical conditions for their existence and localization. Here, by *explicit* we mean that these edge-mode solutions take the form that does not depend on the energy and thus can be determined without solving numerically the large Hamiltonian matrix for energy spectrum, which is usually time-consuming and even incorrect when the matrix dimension is very high [39]. Obviously, these explicit edge-mode solutions may facilitate experimental studies of the underlying BBC for topologically protected edge states in a wide range of non-Hermitian systems [37,38,43,44].

Further, considering that the BBC is a subtle issue that has so far remained in debate for non-Hermitian systems [42,49,74], even on experimental sides [43,44], we expect that the current paper may clarify this disputable issue from the analytical standpoint and open avenues for understanding the elusive non-Hermitian topology in a unified manner.

## ACKNOWLEDGMENTS

This work was supported by the National Natural Science Foundation of China (Grants No. 11974075, No. 12122407, No. 12074308, and No. 12034013) and the National Key Research and Development Program of China (Grant No. 2021YFA1200700). L.Y. thanks Yangyang Development Fund for sponsorship.


## APPENDIX A: ENERGY SPECTRA AND EIGENSTATES UNDER THE PERIODIC BOUNDARY CONDITION

In this Appendix, we would like to present the analytical solutions for the non-Hermitian Hamiltonian under the PBC, which means that the chain shown in Fig. 1(a) is now joined, end to end, to form a loop. For such a loop-type chain, the Hamiltonian Eq. (1) needs to be slightly modified as

$$\hat{H} = \sum_{n=1}^{N}[t_{1L}\hat{c}_{nA}^{\dagger}\hat{c}_{nB} + t_{1R}\hat{c}_{nB}^{\dagger}\hat{c}_{nA} + t_{2L}\hat{c}_{nB}^{\dagger}\hat{c}_{(n+1)A} + t_{2R}\hat{c}_{(n+1)A}^{\dagger}\hat{c}_{nB} + t_{3L}\hat{c}_{nA}^{\dagger}\hat{c}_{(n+1)B} + t_{3R}\hat{c}_{(n+1)B}^{\dagger}\hat{c}_{nA}], \quad \text{(A1)}$$

with $\hat{c}_{(N+1)A} = \hat{c}_{1A}$ and $\hat{c}_{(N+1)B} = \hat{c}_{1B}$. In this situation, the eigenvalue equation $\hat{H}|\psi\rangle = E|\psi\rangle$, with $|\psi\rangle = \sum_{m=1}^{2N}\psi_m|m\rangle = (\psi_{1A}, \psi_{1B}, \cdots, \psi_{NA}, \psi_{NB})^{\mathrm{T}}$, yields a series of bulk equations,

$$t_{1L}\psi_{(n+1)B} + t_{2R}\psi_{nB} + t_{3L}\psi_{(n+2)B} = E\psi_{(n+1)A}, \quad \text{(A2)}$$

$$t_{1R}\psi_{(n+1)A} + t_{2L}\psi_{(n+2)A} + t_{3R}\psi_{nA} = E\psi_{(n+1)B}, \quad \text{(A3)}$$

for $n = 1, \cdots, N$, under the following boundary conditions:

$$\psi_{(N+j)A} = \psi_{jA}, \quad \psi_{(N+j)B} = \psi_{jB}, \quad (j \in \mathbb{N}), \quad \text{(A4)}$$

It follows easily that the $k$th set of solutions satisfying Eqs. (A2)–(A4) can be expressed as

$$\psi_{nA}^{(k)} = c\sqrt{\frac{R_+(\beta_k)}{R_-(\beta_k)}}\beta_k^n, \quad \psi_{nB}^{(k)} = c\beta_k^n, \quad \text{(A5)}$$

for the energy

$$E_k^+ = \sqrt{R_+(\beta_k)R_-(\beta_k)}, \quad \text{(A6)}$$

or given by

$$\psi_{nA}^{(k)} = c\sqrt{\frac{R_+(\beta_k)}{R_-(\beta_k)}}\beta_k^n, \quad \psi_{nB}^{(k)} = -c\beta_k^n, \quad \text{(A7)}$$

for the energy

$$E_k^- = -\sqrt{R_+(\beta_k)R_-(\beta_k)}, \quad \text{(A8)}$$

where $R_+(\beta)$ and $R_-(\beta)$ are the same functions as defined in Eq. (2), $c = \sqrt{|R_-(\beta_k)|/[N(|R_+(\beta_k)| + |R_-(\beta_k)|)]}$, and

$$\beta_k = \exp(ik), \quad \text{with } k \in \left\{\frac{2\pi}{N}, \frac{4\pi}{N}, \frac{6\pi}{N}\cdots, \frac{2N\pi}{N}\right\}. \quad \text{(A9)}$$

Obviously, all $2N$ eigenstates, Eqs. (A5) and (A7), and the corresponding energy spectra, Eqs. (A6) and (A8), are solely determined by the discrete $\beta_k$ values defined by Eqs. (A9).

Then the Bloch Hamiltonian $\mathcal{H}(k)$ resulting from the Fourier transformation of the real-space Hamiltonian (A1) can still be given by Eq. (2), but with the wavenumber $k$ being real and taken from the first BZ. In the complex plane, this BZ will show a unit circle in the thermodynamic limit because of $|\beta_k| = 1$. As a result, the associated energy spectra $E_k$ would trace one or several closed loops in the complex energy plane, different from those allowed by OBC [58]. One can refer to Figs. 2(c), 2(g), 2(k), and 4(b) for a clear picture on these PBC spectra, when compared to the OBC spectra.

## APPENDIX B: SOLVING THE EIGENVALUE EQUATION UNDER OPEN BOUNDARY CONDITION

In this Appendix, let us outline the derivation of Eqs. (5)–(8), starting from the eigenvalue equation $\hat{H}|\psi\rangle = E|\psi\rangle$, where $\hat{H}$ is the real Hamiltonian Eq. (1), $E$ is the energy spectrum, and $|\psi\rangle = \sum_{m=1}^{2N}\psi_m|m\rangle = (\psi_{1A}, \psi_{1B}, \cdots, \psi_{NA}, \psi_{NB})^{\mathrm{T}}$ denotes the corresponding eigenvector, as stated in Sec. II. In the above basis, this eigenvalue equation can again be transformed into a series of bulk Eqs. (A2) and (A3), where now $1 \leqslant n \leqslant N-2$, together with a set of boundary equations:

$$t_{1L}\psi_{1B} + t_{3L}\psi_{2B} = E\psi_{1A}, \quad \text{(B1)}$$

$$t_{1R}\psi_{1A} + t_{2L}\psi_{2A} = E\psi_{1B}, \quad \text{(B2)}$$

$$t_{1L}\psi_{NB} + t_{2R}\psi_{(N-1)B} = E\psi_{NA}, \quad \text{(B3)}$$

$$t_{1R}\psi_{NA} + t_{3R}\psi_{(N-1)A} = E\psi_{NB}. \quad \text{(B4)}$$

Considering the spatial translational invariance of the bulk Eqs. (A2) and (A3), one can assume $\psi_{nA}$ and $\psi_{nB}$ to take the ansatz Eqs. (4), with the energy $E$ determined by Eq. (3). As one can check, the solutions Eqs. (4) enable the bulk Eqs. (A2) and (A3) to hold entirely, and meanwhile transform the boundary Eqs. (B1)–(B4) into the system of linear equations $\mathbf{Rc} = 0$, where $\mathbf{c} = (c_1, c_2, c_3, c_4)^{\mathrm{T}}$ and

$$\mathbf{R} = \begin{bmatrix} 1 & 1 & 1 & 1 \\ R_+(\beta_1) & R_+(\beta_2) & R_+(\beta_3) & R_+(\beta_4) \\ \beta_1^{N+1} & \beta_2^{N+1} & \beta_3^{N+1} & \beta_4^{N+1} \\ \beta_1^{N+1}R_+(\beta_1) & \beta_2^{N+1}R_+(\beta_2) & \beta_3^{N+1}R_+(\beta_3) & \beta_4^{N+1}R_+(\beta_4) \end{bmatrix}. \quad \text{(B5)}$$

For $c_j$ to be nontrivial, the coefficient matrix defined by Eq. (B5) must have a zero determinant, resulting in the OBC Eq. (5) that needs to be satisfied by four $\beta_j$. Naturally, under this OBC, the above system of linear equations, $\mathbf{Rc} = 0$, can be solved, giving rise to Eqs. (5)–(8).

## APPENDIX C: DETERMINATION OF GENERALIZED BRILLOUIN ZONE

In Appendix A, we have shown that the BZ of the bulk modes under the PBC will be a unit circle in the complex plane, namely, $|\beta_k| = 1$. Then, when the boundary condition changes from PBC to OBC, what is the shape of the GBZ of the bulk modes and how do we determine it either numerically or analytically? In the current Appendix, let us address these interesting issues.

As a matter of fact, in previous studies [39,72], it was revealed that in the continuum limit, the middle two $\beta$ values allowed will be equal in modulus (say, $|\beta_2| = |\beta_3|$ here) and thus can constitute the GBZ of the bulk modes, which is a closed loop encircling the origin in the complex plane. This can also be seen from Eq. (5), which now, under the leading-order approximation at $N \to \infty$, reduces to

$$\frac{\beta_{12}\beta_{34}}{\beta_{13}\beta_{24}} = \frac{(\beta_2\beta_4)^{N+1}}{(\beta_3\beta_4)^{N+1}} = \left(\frac{\beta_2}{\beta_3}\right)^{N+1}. \tag{C1}$$

Obviously, as the left-hand side of Eq. (C1) does not depend on $N$ but its right-hand side does, this equation could be possible only when $|\beta_2| = |\beta_3|$ holds. Thus, when the energy $E$ runs over the whole continuum, the trajectories of $\beta_2$ and $\beta_3$ form a closed loop in the complex plane. This idea, proposed in Ref. [72], provides a direct way to determine the GBZ numerically. To be specific, one needs first to choose a sufficiently large $N$ and solve the Hamiltonian Eq. (1) for all eigenvalues $E$. Substituting each $E$ value into Eq. (3), one can get the middle two, $\beta_2$ and $\beta_3$, of the four roots. Finally, plotting all $\beta_2$ and $\beta_3$ in the complex plane, one can obtain the resultant numerical GBZ. Naturally, the larger the lattice size used, the more accurate the numerical GBZ, but meanwhile, the higher cost the computation takes.

Here we provide an analytical way to determine GBZ, without solving the Hamiltonian Eq. (1). It is similar to, but simpler than, that proposed in Refs. [39,72]. Indeed, because of $|\beta_2| = |\beta_3|$, we can let $\beta_2 = ze^{-i\theta}$ and $\beta_3 = ze^{i\theta}$, where $\theta \in [0,\ 2\pi)$. Inserting $\beta_2$ and $\beta_3$ into Eq. (3), respectively, and subtracting these two results to eliminate $E$, we obtain

$$z^4 + \frac{\mu}{2\cos\theta}z^3 - \frac{\nu r^4}{2\cos\theta}z - r^4 = 0, \tag{C2}$$

where $r$, $\mu$, and $\nu$ are same as defined above. This real-coefficient quartic equation has the following four roots:

$$z_1 = -P + \frac{1}{2}\sqrt{-4P^2 - 2p_0 + \frac{q_0}{P}} - \frac{\mu}{8\cos\theta}, \tag{C3}$$

$$z_2 = -P - \frac{1}{2}\sqrt{-4P^2 - 2p_0 + \frac{q_0}{P}} - \frac{\mu}{8\cos\theta}, \tag{C4}$$

$$z_3 = P + \frac{1}{2}\sqrt{-4P^2 - 2p_0 - \frac{q_0}{P}} - \frac{\mu}{8\cos\theta}, \tag{C5}$$

$$z_4 = P - \frac{1}{2}\sqrt{-4P^2 - 2p_0 - \frac{q_0}{P}} - \frac{\mu}{8\cos\theta}, \tag{C6}$$

where

$$p_0 = -\frac{3\mu^2}{32\cos^2\theta}, \quad q_0 = \frac{\mu^3}{64\cos^3\theta} - \frac{\nu r^4}{2\cos\theta}, \tag{C7}$$

$$Q = \left(\frac{\Delta_1 + 3\sqrt{-3\Delta}}{2}\right)^{1/3}, \quad P = \frac{\sqrt{3}}{6}\sqrt{Q + \frac{\Delta_0}{Q} - 2p_0}, \tag{C8}$$

$$\Delta_0 = \frac{3r^4}{4}\left(\frac{\mu\nu}{\cos^2\theta} - 16\right), \quad \Delta_1 = \frac{27r^4(\nu^2 r^4 - \mu^2)}{4\cos^2\theta}, \tag{C9}$$

$$\Delta = \frac{4\Delta_0^3 - \Delta_1^2}{27}. \tag{C10}$$

It turns out that as $\theta$ runs from 0 to $2\pi$, excluding the special points $\pi/2$ and $3\pi/2$, either $(z_1e^{-i\theta},\ z_2e^{-i\theta})$ or $(z_3e^{-i\theta},\ z_4e^{-i\theta})$ can trace a closed loop known as the GBZ. In practice, one can use $(z_2e^{-i\theta},\ z_3e^{-i\theta},\ z_4e^{-i\theta})$ to determine the exact GBZ (eGBZ), as $\theta$ runs from $\pi/2$ to $3\pi/2$. The merit of the latter is that there is no need to sort the roots and there are much fewer worthless lines around the GBZ formed. Basically, the eGBZ is the ultimate measure of how accurate the numerical GBZ obtained with a finite $N$ value could really be. As an example, we demonstrate in Fig. 2(j) the comparison of the GBZ that is obtained with a finite $N = 100$ with the eGBZ that is defined by $(z_2e^{-i\theta},\ z_3e^{-i\theta},\ z_4e^{-i\theta})$, under the same parameter condition. It is exhibited that the GBZ is really composed of the $\beta_2$ and $\beta_3$ trajectories that fulfill $|\beta_2| = |\beta_3|$. Moreover, the GBZ obtained with a relatively small lattice size is shown to be very consistent with the eGBZ.


[1] C. M. Bender and S. Boettcher, Real Spectra in Non-Hermitian Hamiltonians Having $\mathcal{PT}$ Symmetry, Phys. Rev. Lett. **80**, 5243 (1998).

[2] H. Cao and J. Wiersig, Dielectric microcavities: Model systems for wave chaos and non-Hermitian physics, Rev. Mod. Phys. **87**, 61 (2015).

[3] V. V. Konotop, J. Yang, and D. A. Zezyulin, Nonlinear waves in $\mathcal{PT}$-symmetric systems, Rev. Mod. Phys. **88**, 035002 (2016).

[4] L. Feng, R. El-Ganainy, and L. Ge, Non-Hermitian photonics based on parity-time symmetry, Nat. Photonics **11**, 752 (2017).

[5] S. Longhi, Parity-time symmetry meets photonics: A new twist in non-Hermitian optics, Europhys. Lett. **120**, 64001 (2017).

[6] R. El-Ganainy, K. G. Makris, M. Khajavikhan, Z. H. Musslimani, S. Rotter, and D. N. Christodoulides, Non-Hermitian physics and PT symmetry, Nat. Phys. **14**, 11 (2018).

[7] M.-A. Miri and A. Alù, Exceptional points in optics and photonics, Science **363**, eaar7709 (2019).

[8] Y. Ashida, Z. Gong, and M. Ueda, Non-Hermitian physics, Adv. Phys. **69**, 249 (2020).

[9] B. Peng, Ş. K. Özdemir, F. Lei, F. Monifi, M. Gianfreda, G. L. Long, S. Fan, F. Nori, C. M. Bender, and L. Yang, Parity–time-symmetric whispering-gallery microcavities, Nat. Phys. **10**, 394 (2014).

[10] L. Lu, Z. Wang, D. Ye, L. Ran, L. Fu, J. D. Joannopoulos, and M. Soljačić, Experimental observation of Weyl points, Science **349**, 622 (2015).

[11] B. Zhen, C. W. Hsu, Y. Igarashi, L. Lu, I. Kaminer, A. Pick, S.-L. Chua, J. D. Joannopoulos, and M. Soljačić, Spawning rings of exceptional points out of Dirac cones, Nature (London) **525**, 354 (2015).

[12] Y. V. Kartashov, V. V. Konotop, and L. Torner, Topological States in Partially-$\mathcal{PT}$-Symmetric Azimuthal Potentials, Phys. Rev. Lett. **115**, 193902 (2015).

[13] H. Zhou, C. Peng, Y. Yoon, C. W. Hsu, K. A. Nelson, L. Fu, J. D. Joannopoulos, M. Soljačić, and B. Zhen, Observation of bulk Fermi arc and polarization half charge from paired exceptional points, Science **359**, 1009 (2018).

[14] A. Cerjan, S. Huang, M. Wang, K. P. Chen, Y. Chong, and M. C. Rechtsman, Experimental realization of a Weyl exceptional ring, Nat. Photonics **13**, 623 (2019).

[15] N. Hatano and D. R. Nelson, Localization Transitions in Non-Hermitian Quantum Mechanics, Phys. Rev. Lett. **77**, 570 (1996).

[16] C. Hang, G. Huang, and V. V. Konotop, $\mathcal{PT}$ Symmetry with a System of Three-Level Atoms, Phys. Rev. Lett. **110**, 083604 (2013).

[17] Z. Zhang, Y. Zhang, J. Sheng, L. Yang, M.-A. Miri, D. N. Christodoulides, B. He, Y. Zhang, and M. Xiao, Observation of Parity-Time Symmetry in Optically Induced Atomic Lattices, Phys. Rev. Lett. **117**, 123601 (2016).

[18] Y. Xu, S.-T. Wang, and L.-M. Duan, Weyl Exceptional Rings in a Three-Dimensional Dissipative Cold Atomic Gas, Phys. Rev. Lett. **118**, 045701 (2017).

[19] D. Cheng, W. Wang, C. Pan, C. Hou, S. Chen, D. Mihalache, and F. Baronio, Photonic rogue waves in a strongly dispersive coupled-cavity array involving self-attractive Kerr nonlinearity, Phys. Rev. A **105**, 013717 (2022).

[20] T. Ozawa, H. M. Price, A. Amo, N. Goldman, M. Hafezi, L. Lu, M. C. Rechtsman, D. Schuster, J. Simon, O. Zilberberg, and I. Carusotto, Topological photonics, Rev. Mod. Phys. **91**, 015006 (2019).

[21] K. Y. Bliokh, D. Leykam, M. Lein, and F. Nori, Topological non-Hermitian origin of surface Maxwell waves, Nat. Commun. **10**, 580 (2019).

[22] H. Zhao, X. Qiao, T. Wu, B. Midya, S. Longhi, and L. Feng, Non-Hermitian topological light steering, Science **365**, 1163 (2019).

[23] Z. Gong, Y. Ashida, K. Kawabata, K. Takasan, S. Higashikawa, and M. Ueda, Topological Phases of Non-Hermitian Systems, Phys. Rev. X **8**, 031079 (2018).

[24] K. Kawabata, K. Shiozaki, M. Ueda, and M. Sato, Symmetry and Topology in Non-Hermitian Physics, Phys. Rev. X **9**, 041015 (2019).

[25] E. J. Bergholtz, J. C. Budich, and F. K. Kunst, Exceptional topology of non-Hermitian systems, Rev. Mod. Phys. **93**, 015005 (2021).

[26] C. Coulais, R. Fleury, and J. van Wezel, Topology and broken Hermiticity, Nat. Phys. **17**, 9 (2021).

[27] M. Parto, Y. G. N. Liu, B. Bahari, M. Khajavikhan, and D. N. Christodoulides, Non-Hermitian and topological photonics: Optics at an exceptional point, Nanophoton. **10**, 403 (2021).

[28] H. Wang, X. Zhang, J. Hua, D. Lei, M. Lu, and Y. Chen, Topological physics of non-Hermitian optics and photonics: A review, J. Opt. **23**, 123001 (2021).

[29] M. S. Rudner and L. S. Levitov, Topological Transition in a Non-Hermitian Quantum Walk, Phys. Rev. Lett. **102**, 065703 (2009).

[30] J. M. Zeuner, M. C. Rechtsman, Y. Plotnik, Y. Lumer, S. Nolte, M. S. Rudner, M. Segev, and A. Szameit, Observation of a Topological Transition in the Bulk of a Non-Hermitian System, Phys. Rev. Lett. **115**, 040402 (2015).

[31] C.-K. Chiu, J. C. Y. Teo, A. P. Schnyder, and S. Ryu, Classification of topological quantum matter with symmetries, Rev. Mod. Phys. **88**, 035005 (2016).

[32] K. Takata and M. Notomi, Photonic Topological Insulating Phase Induced Solely by Gain and Loss, Phys. Rev. Lett. **121**, 213902 (2018).

[33] S. Longhi, Topological Phase Transition in Non-Hermitian Quasicrystals, Phys. Rev. Lett. **122**, 237601 (2019).

[34] H. Shen, B. Zhen, and L. Fu, Topological Band Theory for Non-Hermitian Hamiltonians, Phys. Rev. Lett. **120**, 146402 (2018).

[35] A. Dikopoltsev, T. H. Harder, E. Lustig, O. A. Egorov, J. Beierlein, A. Wolf, Y. Lumer, M. Emmerling, C. Schneider, S. Höfling, M. Segev, and S. Klembt, Topological insulator vertical-cavity laser array, Science **373**, 1514 (2021).

[36] F. K. Kunst, E. Edvardsson, J. C. Budich, and E. J. Bergholtz, Biorthogonal Bulk-Boundary Correspondence in Non-Hermitian Systems, Phys. Rev. Lett. **121**, 026808 (2018).

[37] A. Ghatak, M. Brandenbourger, J. van Wezel, and C. Coulais, Observation of non-Hermitian topology and its bulk-edge correspondence in an active mechanical metamaterial, Proc. Natl. Acad. Sci. USA **117**, 29561 (2020).

[38] L. Xiao, T. Deng, K. Wang, G. Zhu, Z. Wang, W. Yi, and P. Xue, Non-Hermitian bulk-boundary correspondence in quantum dynamics, Nat. Phys. **16**, 761 (2020).

[39] Z. Yang, K. Zhang, C. Fang, and J. Hu, Non-Hermitian Bulk-Boundary Correspondence and Auxiliary Generalized Brillouin Zone Theory, Phys. Rev. Lett. **125**, 226402 (2020).

[40] H.-G. Zirnstein, G. Refael, and B. Rosenow, Bulk-Boundary Correspondence for Non-Hermitian Hamiltonians Via Green Functions, Phys. Rev. Lett. **126**, 216407 (2021).

[41] P. St-Jean, V. Goblot, E. Galopin, A. Lemaître, T. Ozawa, L. Le Gratiet, I. Sagnes, J. Bloch, and A. Amo, Lasing in topological edge states of a one-dimensional lattice, Nat. Photonics **11**, 651 (2017).

[42] T. E. Lee, Anomalous Edge State in a Non-Hermitian Lattice, Phys. Rev. Lett. **116**, 133903 (2016).

[43] T. Helbig, T. Hofmann, S. Imhof, M. Abdelghany, T. Kiessling, L. W. Molenkamp, C. H. Lee, A. Szameit, M. Greiter, and R. Thomale, Generalized bulk-boundary correspondence in non-Hermitian topolectrical circuits, Nat. Phys. **16**, 747 (2020).

[44] K. Sone, Y. Ashida, and T. Sagawa, Exceptional non-Hermitian topological edge mode and its application to active matter, Nat. Commun. **11**, 5745 (2020).

[45] S. Weimann, M. Kremer, Y. Plotnik, Y. Lumer, S. Nolte, K. G. Makris, M. Segev, M. C. Rechtsman, and A. Szameit, Topologically protected bound states in photonic parity-time-symmetric crystals, Nat. Mater. **16**, 433 (2017).

[46] S. Weidemann, M. Kremer, T. Helbig, T. Hofmann, A. Stegmaier, M. Greiter, R. Thomale, and A. Szameit, Topological funneling of light, Science **368**, 311 (2020).

[47] K. Kawabata, T. Bessho, and M. Sato, Classification of Exceptional Points and Non-Hermitian Topological Semimetals, Phys. Rev. Lett. **123**, 066405 (2019).

[48] D. Cheng, B. Peng, M. Xiao, X. Chen, L. Yuan, and S. Fan, Truncation-dependent $\mathcal{PT}$ phase transition for the edge states of a two-dimensional non-Hermitian system, Phys. Rev. B **105**, L201105 (2022).

[49] S. Yao and Z. Wang, Edge States and Topological Invariants of Non-Hermitian Systems, Phys. Rev. Lett. **121**, 086803 (2018).

[50] F. Song, S. Yao, and Z. Wang, Non-Hermitian Skin Effect and Chiral Damping in Open Quantum Systems, Phys. Rev. Lett. **123**, 170401 (2019).

[51] S. Longhi, Probing non-Hermitian skin effect and non-Bloch phase transitions, Phys. Rev. Res. **1**, 023013 (2019).

[52] N. Okuma, K. Kawabata, K. Shiozaki, and M. Sato, Topological Origin of Non-Hermitian Skin Effects, Phys. Rev. Lett. **124**, 086801 (2020).

[53] L. Li, C. H. Lee, S. Mu, and J. Gong, Critical non-Hermitian skin effect, Nat. Commun. **11**, 5491 (2020).

[54] X. Zhu, H. Wang, S. K. Gupta, H. Zhang, B. Xie, M. Lu, and Y. Chen, Photonic non-Hermitian skin effect and non-Bloch bulk-boundary correspondence, Phys. Rev. Res. **2**, 013280 (2020).

[55] S. Longhi, Unraveling the non-Hermitian skin effect in dissipative systems, Phys. Rev. B **102**, 201103(R) (2020).

[56] K. Zhang, Z. Yang, and C. Fang, Universal non-Hermitian skin effect in two and higher dimensions, Nat. Commun. **13**, 2496 (2022).

[57] C. H. Lee, L. Li, and J. Gong, Hybrid Higher-Order Skin-Topological Modes in Nonreciprocal Systems, Phys. Rev. Lett. **123**, 016805 (2019).

[58] K. Zhang, Z. Yang, and C. Fang, Correspondence between Winding Numbers and Skin Modes in Non-Hermitian Systems, Phys. Rev. Lett. **125**, 126402 (2020).

[59] X. Zhang, Y. Tian, J.-H. Jiang, M.-H. Lu, and Y.-F. Chen, Observation of higher-order non-Hermitian skin effect, Nat. Commun. **12**, 5377 (2021).

[60] D. Leykam, K. Y. Bliokh, C. Huang, Y. D. Chong, and F. Nori, Edge Modes, Degeneracies, and Topological Numbers in Non-Hermitian Systems, Phys. Rev. Lett. **118**, 040401 (2017).

[61] W. Song, W. Sun, C. Chen, Q. Song, S. Xiao, S. Zhu, and T. Li, Breakup and Recovery of Topological Zero Modes in Finite Non-Hermitian Optical Lattices, Phys. Rev. Lett. **123**, 165701 (2019).

[62] D. S. Borgnia, A. J. Kruchkov, and R.-J. Slager, Non-Hermitian Boundary Modes and Topology, Phys. Rev. Lett. **124**, 056802 (2020).

[63] L. Xiao, X. Zhan, Z. H. Bian, K. K. Wang, X. Zhang, X. P. Wang, J. Li, K. Mochizuki, D. Kim, N. Kawakami, W. Yi, H. Obuse, B. C. Sanders, and P. Xue, Observation of topological edge states in parity-time-symmetric quantum walks, Nat. Phys. **13**, 1117 (2017).

[64] Ş. K. Özdemir, S. Rotter, F. Nori, and L. Yang, Parity-time symmetry and exceptional points in photonics, Nat. Mater. **18**, 783 (2019).

[65] Z. Yang, A. P. Schnyder, J. Hu, and C.-K. Chiu, Fermion Doubling Theorems in Two-Dimensional Non-Hermitian Systems for Fermi Points and Exceptional Points, Phys. Rev. Lett. **126**, 086401 (2021).

[66] X. Zhan, L. Xiao, Z. Bian, K. Wang, X. Qiu, B. C. Sanders, W. Yi, and P. Xue, Detecting Topological Invariants in Nonunitary Discrete-Time Quantum Walks, Phys. Rev. Lett. **119**, 130501 (2017).

[67] S. Yao, F. Song, and Z. Wang, Non-Hermitian Chern Bands, Phys. Rev. Lett. **121**, 136802 (2018).

[68] F. Song, S. Yao, and Z. Wang, Non-Hermitian Topological Invariants in Real Space, Phys. Rev. Lett. **123**, 246801 (2019).

[69] K. Wang, A. Dutt, K. Y. Yang, C. C. Wojcik, J. Vučković, and S. Fan, Generating arbitrary topological windings of a non-Hermitian band, Science **371**, 1240 (2021).

[70] B. Peng, Ş. K. Özdemira, M. Liertzerb, W. Chena, J. Kramerc, H. Yilmaza, J. Wiersigc, S. Rotterb, and L. Yanga, Chiral modes and directional lasing at exceptional points, Proc. Natl. Acad. Sci. USA **113**, 6845 (2016).

[71] W. Chen, Ş. K. Özdemir, G. Zhao, J. Wiersig, and L. Yang, Exceptional points enhance sensing in an optical microcavity, Nature (London) **548**, 192 (2017).

[72] K. Yokomizo and S. Murakami, Non-Bloch Band Theory of Non-Hermitian Systems, Phys. Rev. Lett. **123**, 066404 (2019).

[73] C.-X. Guo, C.-H. Liu, X.-M. Zhao, Y. Liu, and S. Chen, Exact Solution of Non-Hermitian Systems with Generalized Boundary Conditions: Size-Dependent Boundary Effect and Fragility of the Skin Effect, Phys. Rev. Lett. **127**, 116801 (2021).

[74] Y. Xiong, Why does bulk boundary correspondence fail in some non-hermitian topological models, J. Phys. Commun. **2**, 035043 (2018).

[75] W. P. Su, J. R. Schrieffer, and A. J. Heeger, Solitons in Polyacetylene, Phys. Rev. Lett. **42**, 1698 (1979).

[76] L. Li, Z. Xu, and S. Chen, Topological phases of generalized Su-Schrieffer-Heeger models, Phys. Rev. B **89**, 085111 (2014).

[77] M. Bello, G. Platero, J. I. Cirac, and A. González-Tudela, Unconventional quantum optics in topological waveguide QED, Sci. Adv. **5**, eaaw0297 (2019).

[78] C. Poli, M. Bellec, U. Kuhl, F. Mortessagne, and H. Schomerus, Selective enhancement of topologically induced interface states in a dielectric resonator chain, Nat. Commun. **6**, 6710 (2015).

[79] M. Parto, S. Wittek, H. Hodaei, G. Harari, M. A. Bandres, J. Ren, M. C. Rechtsman, M. Segev, D. N. Christodoulides, and M. Khajavikhan, Edge-Mode Lasing in 1D Topological Active Arrays, Phys. Rev. Lett. **120**, 113901 (2018).

[80] S. Longhi, Non-Hermitian gauged topological laser arrays, Ann. Phys. **530**, 1800023 (2018).

[81] C. H. Lee, S. Imhof, C. Berger, F. Bayer, J. Brehm, L. W. Molenkamp, T. Kiessling, and R. Thomale, Topolectrical circuits, Commun. Phys. **1**, 39 (2018).

[82] S. Liu, R. Shao, S. Ma, L. Zhang, O. You, H. Wu, Y. J. Xiang, T. J. Cui, and S. Zhang, Non-Hermitian skin effect in a non-Hermitian electrical circuit, Research **2021**, 5608038 (2021).

[83] W. Zhang, X. Ouyang, X. Huang, X. Wang, H. Zhang, Y. Yu, X. Chang, Y. Liu, D.-L. Deng, and L.-M. Duan, Observation of Non-Hermitian Topology with Nonunitary Dynamics of Solid-State Spins, Phys. Rev. Lett. **127**, 090501 (2021).

[84] J. K. Asbóth, L. Oroszlány, and A. Pályi, *A Short Course on Topological Insulators* (Springer, Cham, 2016).

[85] I. S. Gradshteyn and I. M. Ryzhik, *Table of Integrals, Series, and Products*, edited by D. Zwillinger and V. Moll, 8th ed. (Academic, San Diego, 2014), Chap. 8.